Scanning and Tunable Micro-Optics for Endoscopic Optical Coherence Tomography

K. Aljasem, L. Froehly, A. Seifert, H. Zappe

Scanning and Tunable Micro-Optics for Endoscopic Optical Coherence Tomography

Khaled Aljasem, Luc Froehly, Andreas Seifert, and Hans Zappe, *Member, IEEE*

***Abstract*—The design, fabrication, and integration of micro-optical components for beam focus and steering are demonstrated in an endoscopic optical coherence tomography (OCT) system. The relevant components, a membrane-based microfluidic tunable microlens and an electrostatic 2-D scanning micromirror, are fabricated using silicon and polymer-based microelectromechanical system technologies. All components are assembled inside a 4.5 μm diameter probe. The design of the optical system, including substantiation of the need for focal length tunability, is presented, along with performance data of an OCT system using these components. A lateral resolution of about 13 μm is achieved, an improvement over fixed-focal length probes. Due to the miniaturization of the measurement head achievable using this optical microsystem, use in conventional endoscopes is possible. [2011-0016]**

***Index Terms*—Endoscopic imaging, endoscopic optical coherence tomography, microlenses, micromirrors, tunable micro-optics.**

I. Introduction

OPTICAL coherence tomography (OCT) is a high-resolution optical technique for cross-sectional imaging of semitransparent biological tissue. Due to its high-resolution and noninvasive character, its utility has been demonstrated in a wide range of clinical and medical applications [1]. As an extension of this technology, endoscopic OCT is currently under development as a primary tool for minimally invasive optical biopsies. Three-dimensional (3-D) subsurface mapping of biological tissue allows precise localization, and analysis of abnormalities beneath the surface and microsystems engineering as well as microelectromechanical system (MEMS) technology has been employed for the fabrication of miniaturized scanning micromirrors for 3-D imaging using endoscopic OCT implementations [2]–[4].

Microsystem technology has enabled the realization of miniaturized MEMS-based scanners [2], [5], [6], which allow beam steering without rotation of the entire catheter, as is the case for currently employed clinical systems [7]. MEMS components for rapid scanning have been demonstrated in OCT systems, but issues such as biocompatibility, linearity, reproducibility, and repeatability still require further development. These currently applied endoscopic configurations use fixed-focal length lenses and thus suffer from limitations in performance. If the focus of the measurement beam is fixed, the endoscope must be positioned precisely with respect to the tissue surface, usually a difficult undertaking. In addition, and more significantly, the image quality degrades rapidly for structures removed from the focal point, due to the divergence of the Gaussian measurement beam. As a result, optimal imaging can only be performed for a limited range of longitudinal scanning positions unless the focal point can be tuned with the longitudinal scan. Several MEMS-based approaches for the realization of dynamic focus systems have been proposed [8], [9], albeit only in macroscopic dimensions and without quantitative optical characterization. We demonstrate here an endoscopic OCT system with a tunable objective lens system and a 2-D scanning micromirror, both miniaturized and integrated into a microsystem with a diameter of less than 4.5 mm. Both the miniaturization, leading to a system size compatible with standard endoscopes, and the combination of tunable membrane lenses and scanning micromirrors are shown here for the first time.

Beginning with a brief survey of previous work in this area, we describe the design and fabrication of the tunable microlens system, including quantitative optical characterization. Following a discussion of the scanning micromirror, these structures are used in Fourier domain, time domain with axial scan priority, and time domain with lateral scan priority (en-face) OCT systems.

II. OCT Principles and Implementations

OCT is a form of white-light interferometry. The simplest configuration of the systems is based on a Michelson interferometer, as shown schematically in Fig. 1. The interferometer uses a broad-band super-luminescent SLED with a center wavelength of 1300 nm and bandwidth of 40 nm, the light from which is directed into a measurement and a reference arm. In heterodyne-based time-domain OCT (TD-OCT), an interference signal is only generated when the optical path lengths of the two arms are equal; the reference arm is thus scanned, resulting in interference from reflections at different depths in a material placed in the measurement arm. As a result, a reflection profile below the surface of a material may be generated, allowing nondestructive imaging of subsurface features.

Key to the use of such an OCT system endoscopically is the ability to place the measurement head, shown in Fig. 1(b),

K. Aljasem, A. Seifert, and H. Zappe are with the Laboratory for Micro-optics, Department of Microsystems Engineering, University of Freiburg, 79110 Freiburg, Germany (e-mail: aljasem@imtek.uni-freiburg.de; aljasem@imtek.de; andreas.seifert@imtek.uni-freiburg.de; zappe@imtek.uni-freiburg.de).

L. Froehly is with the Département d'Optique, Université Franche-Comté, 25030 Besancon, France (e-mail: luc.froehly@univ-fcomte.fr).

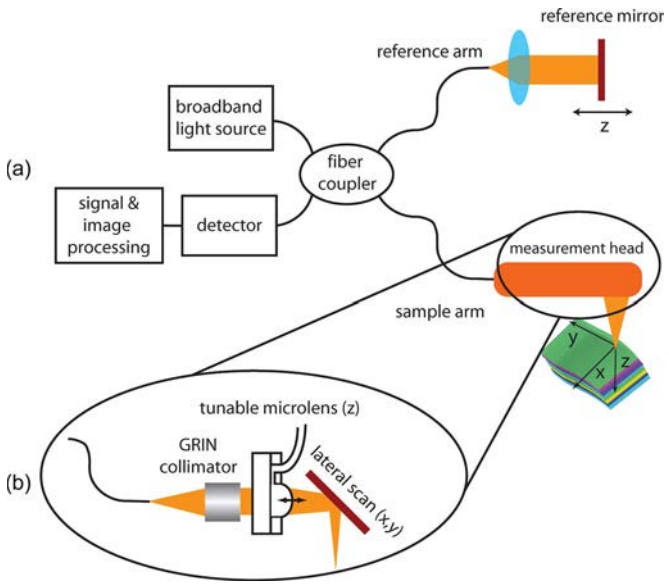

Fig. 1. (a) Schematic diagram of a time-domain OCT system based on a Michelson interferometer in which the reference arm is scanned. (b) The measurement arm presented here contains a MEMS-based tunable objective and a scanning micromirror, miniaturized so as to fit inside an endoscope. Endoscopic applications tend to use 1300 nm radiation with bandwidths of 20–200 nm.

inside an endoscope, which has a diameter of typically less than 5 mm. This measurement head needs to include optics for beam collimation, a tunable objective (a two lens system in our case), and a 2-D scanning micromirror. It is the design, fabrication, assembly, and characterization of this miniaturized measurement head which form the focus of the work presented here.

A. System Variations

The system shown in Fig. 1 represents TD-OCT, in which a scan of the reference arm results in a depth scan into the measurement sample, the so-called A-scan, which defines the Z-axis in the OCT configuration of Fig. 1. Two or 3-D images can be obtained if the measurement beam is laterally deflected by the micromirror after an A-scan, yielding the B- and C-scans. The complete image is then assembled as a one or 2-D array of depth scans. A variation of this scanning approach is en-face OCT, which yields images in time domain. In this approach, the lateral (B and C) scans are completed and then the A-scan increments by one small depth step [10]–[14]. The resultant image is thus assembled as a sequence of planes, each plane at a different depth. En-face OCT is preferable when detailed information from a single plane is required or for a system in which the speed of the A-scan is limited, as for our implementation using the dynamically focusing microlens.

Finally, Fourier-domain OCT (FD-OCT) does not require a longitudinal scan of the reference arm, but instead relies on a grating which disperses the light reflected from the measurement arm onto a linear detector array [15]; many current clinical implementations also use tunable lasers to sweep the wavelength, rather than using broadband emission with a dispersive grating. Taking the spatial Fourier transform of the resultant intensity distribution allows reconstruction of the depth information. In addition to improved sensitivity over time-domain approaches, FD-OCT systems enable fast imaging such that functional parameters have been successfully measured using FD-OCT techniques [16]. We will look at this technique in greater detail in Section VII-D below.

B. Advantage of Tunability

One of the key features of the OCT configuration we present here is the incorporation of a tunable objective using a tunable microlens. As argued in Section I, dynamically scanning the position of the focal point with the A-scan results in improved depth resolution and thus considerably enhanced imaging quality.

We may see this effect explicitly by considering the most important optical parameters of the system [17]. The lateral resolution Δx given by

$$\Delta x = \frac{4\lambda}{\pi} \cdot \frac{f}{d} \tag{1}$$

defines the smallest lateral (in the direction of the B and C-scans) structure which may be imaged by the system; a small value for Δx implies high resolution. Similarly, the axial resolution Δz given by

$$\Delta z = \frac{1}{2} \cdot L_c \approx 0.44 \cdot \frac{\lambda^2}{\Delta\lambda} \tag{2}$$

defines the smallest longitudinal (in the direction of the A-scan) structure which may be resolved; again, we prefer a small value for Δz for high resolution. Finally, the depth of focus DOF,

$$DOF = \frac{\pi \Delta x^2}{2\lambda} \tag{3}$$

defines the axial extent of the beam waist; we prefer a large value for DOF since this implies a large scannable depth range. In the previous expressions, f and d represent the focal length and the aperture of the imaging lens system, λ is the wavelength, $\Delta\lambda$ the SLED bandwidth, and L_c its coherence length. For a given λ, (1) and (2) show that axial and lateral resolutions are independent. In contrast, (1) and (3) reveal that Δx and DOF are directly related: a large depth of focus (and thus depth range) implies a large Δx and thus small lateral resolution, or, inversely, high resolution leads to a limited usable depth range. For a fixed focal length OCT measurement head, then, the optical design must be chosen to provide a compromise between DOF and Δx. A tunable objective allows us to circumvent this limitation: by designing the system for small Δx (high resolution) and small DOF, the position of the focal point is scanned concomitantly with the A-scan. Thus, high resolution is maintained for the entire depth scan, which is ultimately limited by absorption and scattering in the measurement sample.

III. Tunable Microlens

To enable tunability of the focal point during the A-scan, the endoscopic measurement head was designed with a tunable objective, consisting of a tunable microlens combined with

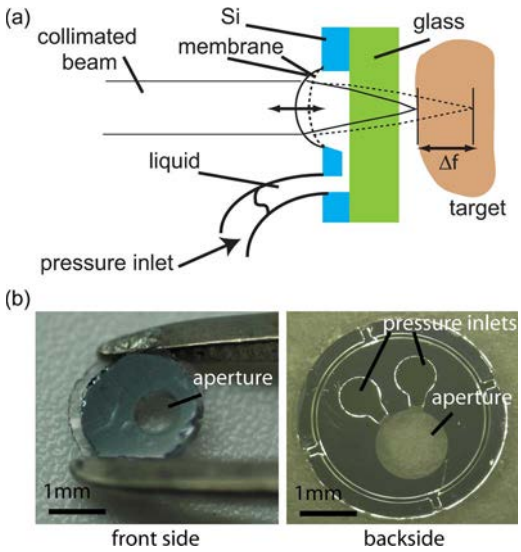

Fig. 2. (a) Schematic cross section of the tunable microlens. The microlens is actuated by applying a pneumatic pressure to the liquid in the lens cavity, resulting in a change of the lens curvature and thereby changing the focal length, seen as the difference between the dashed and continuous lines. (b) Top and bottom views of the Si substrate of the microlens; the substrate has a diameter of 3 mm and an aperture of 1 mm.

a fixed focal length microlens. The variable microlens was based on the membrane-based pressure-tunable lens described previously [18].

A. *Design and Fabrication*

The membrane-based microlens consists of three levels: a transparent, highly elastic membrane, a microfluidic platform based on a silicon substrate, and a glass backing plate. As shown schematically in Fig. 2, a 60 μm thick polydimethylsiloxane (PDMS) membrane is spun onto an approximately 400 μm thick Si substrate with an etched circular opening in the center, representing the lens aperture. The PDMS membrane consisted of a 60 μm thin Silgard 186 silicone elastomer from Dow Corning and has previously been shown to be usable as an etch stop for ICP etch. A microfluidic network is etched from the back side of the Si wafer and a 2 mm thick borosilicate glass (BK7) plate is glued to this using UV-curable adhesives to seal the lens.

The lens cavity is filled with an optical liquid (a water/ethanol mixture, with $n = 1.3534$ at the operating wavelength). By varying the pressure on this liquid, the distension of the membrane is varied, the latter defining the refractive lens surface. As a result, the lens is tuned pneumatically; pneumatic actuation is widely used in clinical endoscopy for diagnostics and therapy, particularly in otology and gastroenterology [19]–[21], such that this approach is compatible with standard endoscopic procedures. Changing the focal point, while keeping the diameter of the beam constant, leads to a change of the numerical aperture (NA), and hence a change of resolution. Nevertheless, the tuning is accomplished without the need to physically move optical components with respect to each other, strongly simplifying the system and permitting miniaturization.

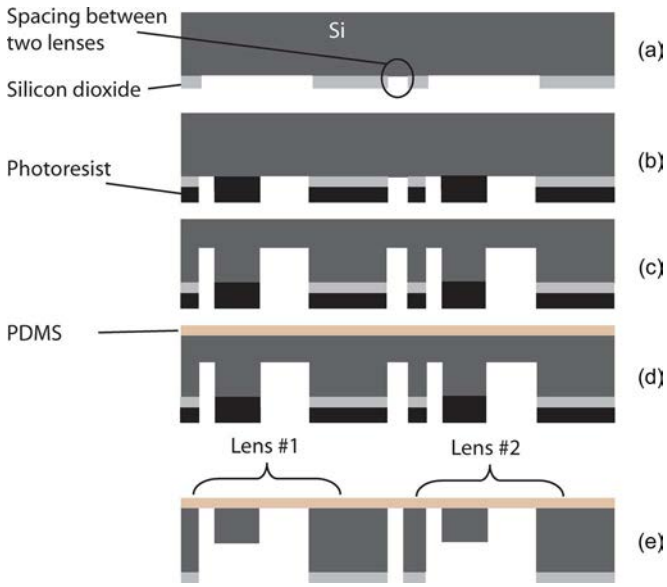

Fig. 3. Fabrication steps to form the cavities on the backside of the Si substrate. (a) Oxide mask for the lens cavity and aperture. (b) Photoresist mask to define the aperture. (c) First 200 μm deep DRIE step to half the depth of the aperture. (d) Spin coating of PDMS onto the front side of the wafer. (e) Second DRIE step to create the aperture and the lens cavity. The spin coating of the PDMS is carried out before the second ICP etch process; subsequently, the membrane functions as an etch stop layer.

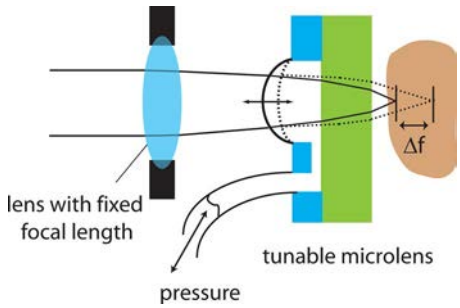

Fig. 4. Multimicrolens system: a lens with a fixed focal length is placed in front of the tunable microlens, resulting in reduced spherical aberration and improved MTF. An achromatic lens from Linos with 40 mm fixed focal length is used in this configuration.

The fabrication process of the PDMS-silicon hybrid technology has been described previously [18] and briefly summarized in Fig. 3.

B. *Multimicrolens System*

As will be seen in the discussion of lens characterization in Section IV below, the optical properties of the objective are significantly improved by using a two-lens system, thus combining the tunable microlens with a fixed focal length lens; Fig. 4 shows this concept. The fixed focal length lens, with a focal length of 40 mm, focuses the beam slightly before it passes through the tunable lens. This configuration allows the tunable lens to be used with a smaller portion of its aperture, without decreasing the NA of the system, and thus minimize the effect of spherical aberration while enhancing the system modulation transfer function (MTF).

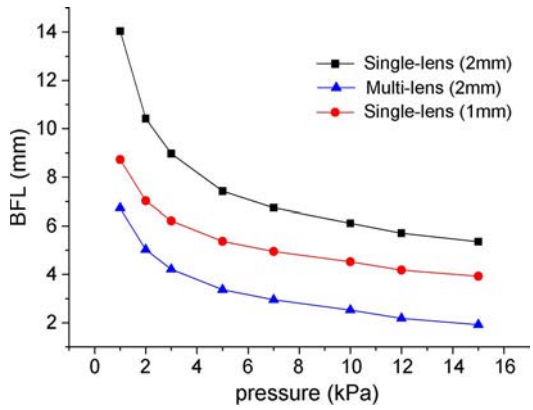

Fig. 5. Variation of back-focal length with pressure for the 2 mm lens as a single-lens and in a multilens system, for the range 1 kPa and 15 kPa. The calibration curve of the 1 mm lens integrated in the probe design of Fig. 13 is also shown.

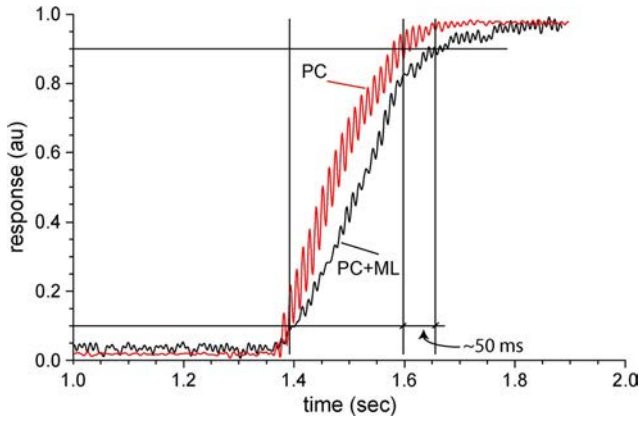

Fig. 6. Time response of the tunable system with and without the microlens. The time constants (t_{PC} and t_{PC+ML}) correspond to the pressure controller (PC) alone and the PC including the tunable microlens (PC+ML), respectively. The experiment was done by decreasing the pressure from 10 kPa to 6 kPa.

IV. Microlens Characterization

For use in an endoscopic OCT system, the tunable lens and the two-lens combination require optimized optical characteristics. We therefore discuss here the focal length tuning, dynamic response, and lateral resolution in more detail.

A. Focal Length Tuning

The change of the focal length is due to the variation of the membrane curvature with pressure. Fig. 5 shows the variation of back-focal length (BFL) of the lens as a function of pressure for 1 mm and 2 mm lens apertures. For the latter, the BFL curves are given for a single lens system and a multilens system.

Whereas the tuning range of the single lens with 2 mm aperture is about 8 mm, the multilens system shown here is optimized for 5 mm, so that the change of the focal point is less sensitive to the variation of the applied pressure. This value is significantly larger than the typical depth range of an OCT A-scan, generally 1–3 mm, such that the focal point can track the entire scan. The endoscopic system requires only a small change in focal length, but a fast response and repeatable characteristics.

B. Dynamic Response

The dynamic behavior, or time response, of the lens was characterized by measuring the change of intensity at a detector which was placed so as to have its full aperture illuminated by the optical field generated by the lens. When the focal length, and thus the lateral size of this optical field, was varied by changing the pressure using an external controller (DPI 520 from Druck Ltd.), the resulting change in detector current is a direct function of the change in lens membrane shape.

The dynamic response of the lens itself was determined by comparing the pressure response of the system (pressure controller (PC), connecting tubes, and lens), once including the lens and once with the lens replaced by a pressure sensor (Motorola MPX5050). Fig. 6 compares the time response of the two cases, once for the PC with tubing plus microlens (PC+ML), measured using the photodetector, and once for just the PC with tubing, measured using the pressure sensor; the former case yields a 10%–90% response time of 250 ms, and the latter a response time of 200 ms. We see thus that the lens adds about 50 ms to the response time and that the entire system may be operated at an actuation frequency of not more than about 4 Hz (1/250 ms).

Since the A-scan is performed at kilohertz rates in advanced OCT systems, the limited dynamic response of the tunable microlens implies that the focal length cannot be tuned concomitantly with a standard depth scan, as we will discuss further in Section VII-B below. En-face OCT systems, on the other hand, perform lateral scans at a fixed depth before incrementing the A-scan, such that the tunable lens is optimal for this type of OCT implementation.

C. Lateral Resolution

The diffraction-limited lateral resolution of the objective lens system, Δx as given in (1), is an important optical parameter since this ultimately defines the smallest features visible in an OCT image. The characteristic resolution of an objective lens is best characterized by the MTF, which relates image contrast to feature size.

MTF is determined through a measurement of the lens profile and a subsequent fit of this profile by an eight order polynomial [22]; these coefficients are used as input to ray-tracing software (Zemax) which is used to calculate the MTF value. Performed at a variety of pressure values, this approach allows determination of MTF as a function of focal length for the tunable lens as well as the two-lens combination.

Based on this approach, each graph in Fig. 7 shows the MTF curves of the tunable single-lens system and the combined two-lens system, for four applied pressure values and thus focal lengths. Using the criterion that the resolution limit is derived as when MTF decreases to 0.5, the lateral resolution of the tunable single lens is about 30 μm. The lateral resolution of the two-lens system is significantly improved and is between 15 μm and 20 μm for all focal lengths examined. As a result, the two lens system provides considerably improved MTF when compared with a single tunable lens, such that the endoscopic

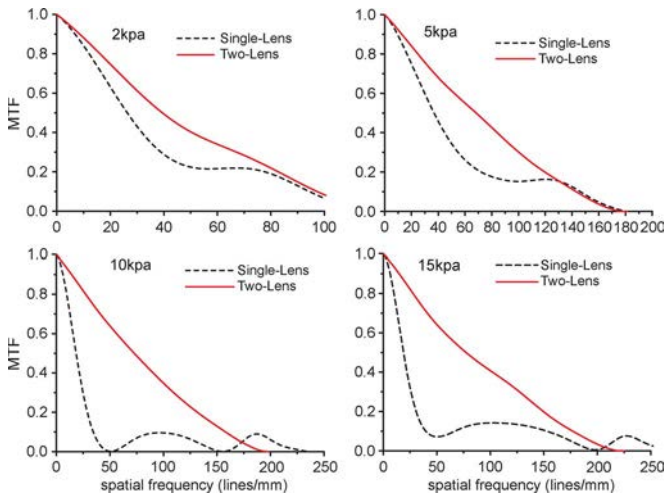

Fig. 7. Modulation transfer function of the single tunable lens with 2 mm aperture and the two-lens system at four pressures (1, 7, 10, and 15 kPa). The incident beam diameter is 1.4 mm. A fixed-focal length objective lens of 40 mm focal length was used for the simulation at a wavelength of 1300 nm. The slope of the MTF curves changes when varying the wavelength, but the improvement of the lateral resolution of the two-lens system is still seen. The above parameters are used for the simulations below.

system will employ the dual-lens variant to assure maximum resolution performance.

V. Scanning Micromirror

The second microsystem component included in the endoscopic system is the scanning micromirror, used for lateral scanning and thus generation of 2-D and 3-D images. The mirror is electrostatically actuated and designed as a parallel-plate system, which leads to a high fill factor. Electrostatic actuation allows fast scanning rates with very low power consumption.

A. Design and Dimensions

The scanning micromirror consists of a square torsional mirror plate, monolithically integrated into a single crystal Si substrate. The two inner meander-shaped torsional beams suspend the mirror from the gimbal, and the orthogonal outer beams suspend the gimbal from the Si substrate, as seen in Fig. 8. The electrodes are positioned below the mirror. The mirror, the gimbal, and the torsional beams are between 5 μm and 10 μm thick; the Si frame is of standard wafer thickness, about 280 μm.

As can be seen in Fig. 9, the fabrication of the mirror uses standard bulk micromachining technology, employing an anisotropic etch of Si from both sides of the Si wafer [23]. The wafer is thinned to 170 μm to reduce the spacing between the electrodes and the mirror, thereby minimizing the voltage required for tilting the mirror. The electrodes are fabricated by standard lithography of a metal layer deposited on the silicon. The mirror and electrode substrates are bonded using high precision flip-chip bonder with an alignment tolerance of less than 10 μm.

To combine the mirror with the tunable microlens for high lateral-resolution imaging, the mirror has to be as large as possible to yield a high NA. Therefore, the size of the chip represents

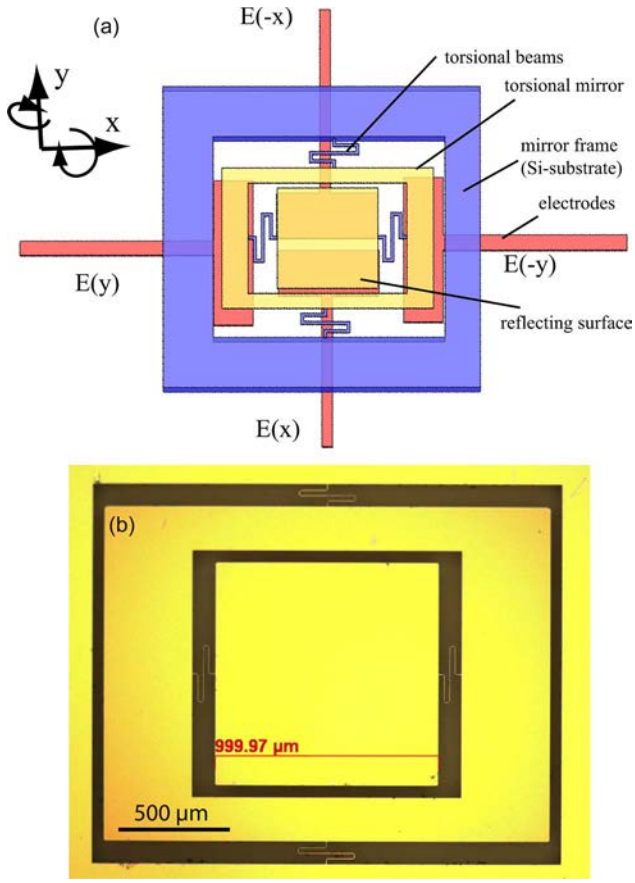

Fig. 8. (a) Schematic view of the scanning mirror, including the Si substrate and the electrodes; the mirror is tilted around the torsional beams when a voltage is applied to one of the four electrodes. b) Top view of the fabricated mirror, in which the support beams are clearly seen.

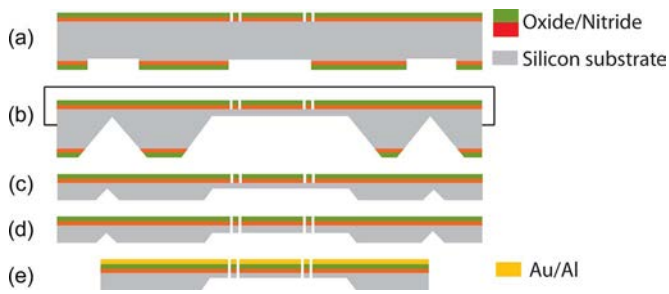

Fig. 9. Fabrication process chain for the tilt mirror. Process description. (a) Defining the mirror structures on the passivation layer on both sides of the substrate. (b) KOH etch from the backside of the Si substrate. (c) Wafer thinning (optional) and chip separation. (e) ICP etch from the front side of the mirror. (f) Deposition of a gold layer to improve the reflectivity of the mirror.

a tradeoff between the achievable lateral resolution and the size of the measurement head. For endoscopic integration, a 2.5 mm $\times$ 3 mm chip size with a 1 mm $\times$ 1 mm active mirror surface is an optimal size. For simplicity, we refer to the areas of the mirrors by their widths.

B. Characterization

Fig. 10 shows the relationship between applied voltage and tilt angle as a function of several parameters. Fig. 10(a) shows this relation for the mirror (X) and gimbal (Y), Fig. 10(b) this

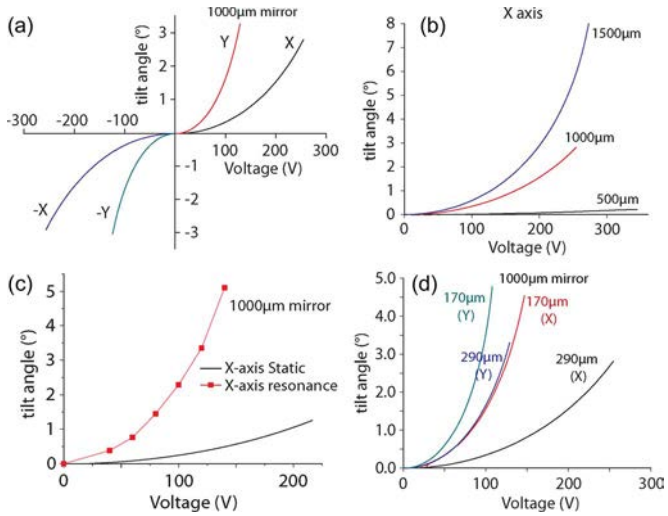

Fig. 10. Tilt angle as a function of actuation voltage for different conditions. (a) Actuation in static mode for the gimbal (Y) and the mirror (X). (b) X-axis actuation for different mirror areas. c) X-axis actuation in static and resonance modes. d) 2-D actuation for a single mirror with different electrode spacings.

TABLE I
CHARACTERISTICS OF A 1-mm SCANNING MIRROR

Parameter	Value
Chip dimensions	2.5 mm×3 mm
Active mirror dimensions	1 mm×1 mm
Resonance frequency (X)	636 Hz
Resonance frequency (Y)	278 Hz
Maximum voltage	∼100 V for ±4° tilt
Roughness	∼3 nm
Radius of curvature	>5 cm
Cross-talk	0.14° in Y-axis for ±4° in X-axis

relation for several widths of the mirror, Fig. 10(c) the relation in static and resonance modes, and Fig. 10(d) for different spacings between the mirror and the electrodes. Based on these characteristics, we chose the 1 mm mirror with a spacing of 170 μm as an optimal design, for which the mirror can be tilted at ±4° for an actuation voltage around 100 V. Table I summarizes the characteristics of this mirror.

VI. ASSEMBLY AND INTEGRATION

A major challenge in the realization of a miniaturized OCT measurement head using the micro-optical devices just described is the integration into a functional microsystem with optimized performance. We discuss optimal placement of the mirror with respect to the microlenses and assembly into a complete system.

A. Optical Optimization

The optical quality of the 3-D scanner is strongly influenced by the placement of the scanning mirror and the microlenses with respect to the incoming collimated beam. As shown in Fig. 11, two basic arrangements are possible: the microlens before the micromirror, or vice-versa. We can characterize the efficacy of these arrangements by modeling the MTF as a function of mirror tilt as it varies from the 45° position.

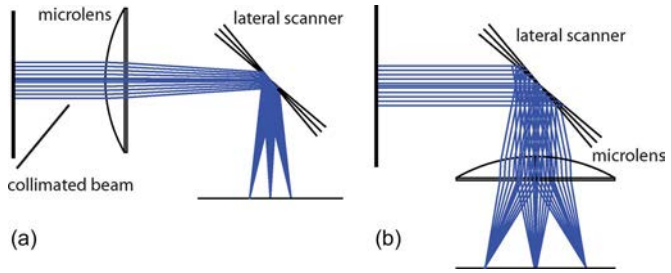

Fig. 11. Two possible arrangements of the 3-D scanner in the sample arm of OCT, the lens-mirror (LM) sequence *left* and mirror-lens (ML) *right*. In both cases, illumination is from the left and image planes at the bottom.

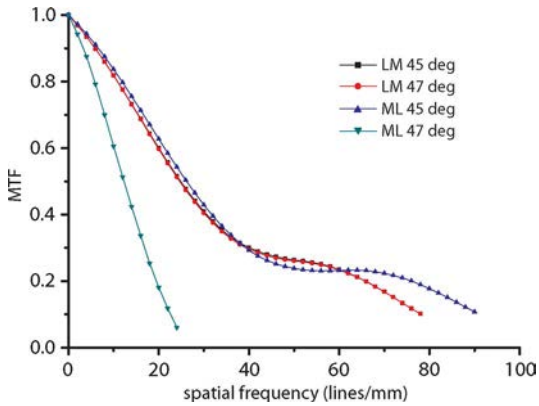

Fig. 12. Calculated MTF for the mirror/lens arrangements shown in Fig. 11. (a) The mirror-lens (ML) sequence with the mirror positioned at exactly 45°. (b) The ML sequence with a mirror tilt of 2° with respect to 45°. (c) The lens-mirror (LM) sequence with the mirror positioned at 45°. (d) The LM arrangement with a mirror tilt of 2° with respect to 45°.

The MTF simulations consider a tunable (single) lens with a 2 mm aperture and a focal length of 11 mm, given by an applied pressure of 2 kPa. Fig. 12 shows the MTF of the optical system for different arrangements: 1) the mirror-lens (ML) sequence with the mirror positioned at exactly 45°; 2) the ML sequence with a mirror tilt of 2° with respect to 45°; 3) the lens-mirror (LM) sequence with the mirror positioned at 45°; and 4) the LM arrangement with a mirror tilt of 2° with respect to 45°.

We see from these results that the MTF of the LM sequence does not change significantly when the mirror tilts by 2°, a typical value during an OCT lateral scan. On the other hand, the MTF of the ML sequence significantly drops when the mirror tilts by this amount, due primarily to the fact that, due to the scan, significantly different portions of the microlens are traversed by the beam, as seen in Fig. 11, such that the effect of aberrations vary strongly with mirror position. As a result, an optimal imaging resolution implies that an optical arrangement involving placement of the microlenses (tunable and fixed-focus lenses) *before* the micromirror in the measurement head is to be preferred.

B. Packaging and Assembly

For the final assembly of the measurement head, the tunable microlens system and the mirror are fixed onto a mechanical body. The tunable microlens portion consists of the microlens bonded onto an aluminum cylinder with three holes, as seen

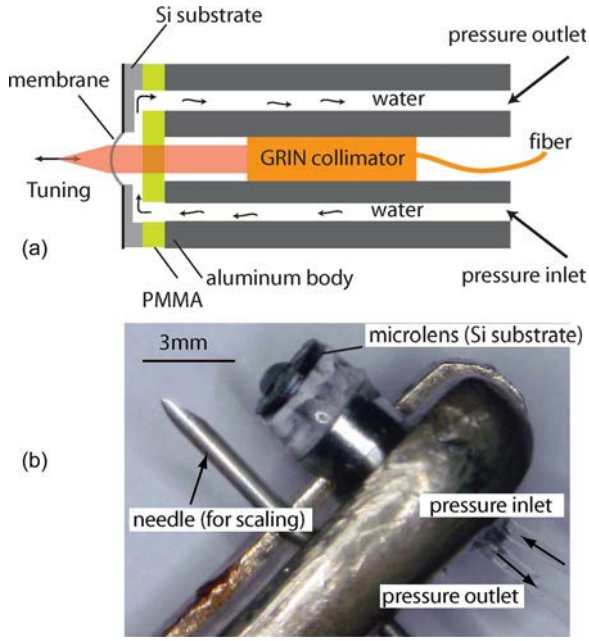

Fig. 13. Schematic design (a) and photograph (b) of the tunable lens arrangement for the measurement head. In (b), the cylinder is held by tweezers, and the arrows at the lower right indicate the hoses for application of pressure to the optical liquid inside the lens.

in Figs. 2(b) and 13(a); one hole is for the optical path and the other two are the pressure inlet and outlet. The two holes of the lens substrate are aligned to the corresponding holes of the cylinder so that the lens aperture is aligned onto the optical axis of the beam exiting the GRIN-lens. The Si/PMMA substrate is fixed to one side of the cylinder, and two pressure tubes are inserted into the other side. To achieve the required miniaturization, a GRIN lens was used as the fixed-focal length lens of the two-lens tunable objective, also inserted into the center of the cylinder, in the optical axis.

Fig. 13(b) shows a photograph of the assembled tunable lens under pressure. Although the tolerance of the alignment was not measured, it is estimated to be less than 20 μm. Based on our simulation results of the single lens and the two-lens systems, this level of uncertainty causes less than 5% degradation of the lateral resolution.

The scanning part of the measurement head consists of the mechanical aluminum body on which the mirror and the electrodes are mounted. The 2.5 mm $\times$ 3 mm mirror chip with a 1 mm $\times$ 1 mm reflecting area is designed for a beam waist of the collimated light beam of 0.7 mm in diameter. Since the mirror chip is initially placed at 45° to the illuminating beam, the projection size of the mirror is reduced by $\sqrt{2}$, still sufficient to reflect the entire beam. The electrical connections to the contact pads are formed using wedge-wedge bonding, where the free ends of the wires are attached to connectors of the driving voltage source. This assembly technique was sufficient to test the probe on the optical measurement bench. Finally, we used UV-curable adhesives to fix the components onto the mechanical body.

The assembly of the entire system, including the GRIN collimator, tunable lens, scanning micromirror, as well as the optical fiber input and pressure connections, is seen in Fig. 14.

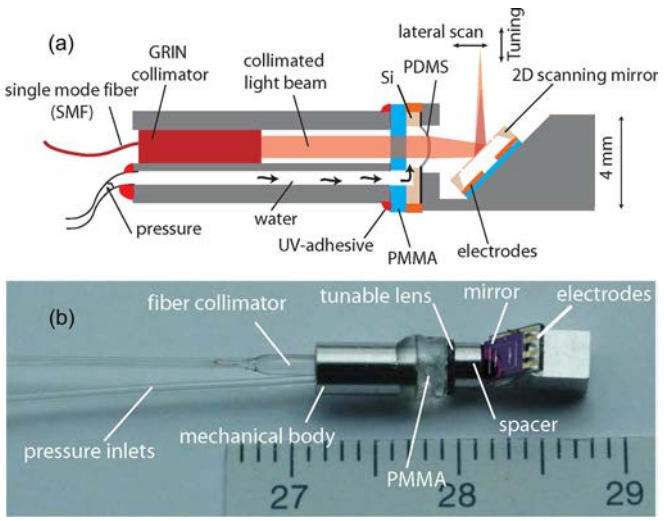

Fig. 14. Schematic design (a) and photograph (b) of the completed measurement head, including the tunable lens arrangement and the scanning micromirror. The relative positions of the GRIN collimator, the tunable lens, the scanning micromirror as well as the optical fiber input and pressure hoses are seen. The outer diameter of the measurement head is 4 mm.

The measurement head is connected to the sample arm of the OCT system by an optical fiber which is connected to the far side of the GRIN collimator. Since this fiber increases the optical path length of the sample arm, the reference arm is extended by another fiber of same length, to compensate the ensuing optical path difference.

VII. Measurement Results

To demonstrate the utility of the assembly, particularly with respect to the optical performance, we have employed several variations of the system in time domain, en-face, and FD-OCT setups. The measurement results show the utility of the tunable objective as well as the integrated scanning micromirror.

A. Time-Domain OCT—Resolution

In the discussion of Section II-B, we argued that a tunable objective would lead to enhanced lateral resolution of the OCT image, if the focal point of the measurement beam were to coincide with the momentary measurement depth within the coherence gate. We can demonstrate quantitatively that this is so by using a TD-OCT setup to measure the MTF of the entire system while varying the spacing between the measurement head and a sample.

Al stripes were microfabricated on a glass with 4 μm to 30 μm lines and spacings, We first used the tunable microlens without the micromirror, instead scanning the target mechanically to realize the B-scan. The image generated by scanning the measurement beam of the TD-OCT setup across a set of 10 μm wide stripes at various sample distances (3.5 to 6 mm) is seen in Fig. 15; the focal length of the tunable objective was adapted (by changing the lens pressure) so that the sample was in focus for each sample distance. We see from the figure that the 10 μm wide stripes are resolved equally well at all sample

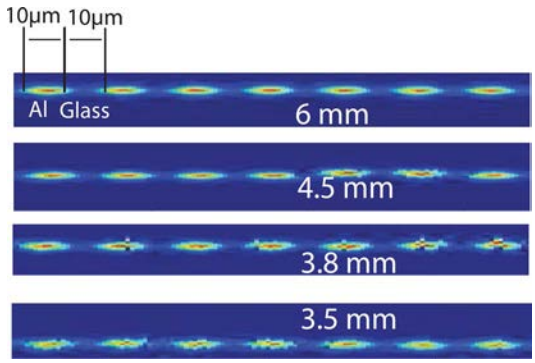

Fig. 15. Four separate TD-OCT images (B-scan) of a linear aluminum-glass grating at various sample distances (6 mm-3.5 mm) showing that the 10 μm stripes are equally resolved as the focal length of the tunable dual objective is varied to adapt to the different sample distances.

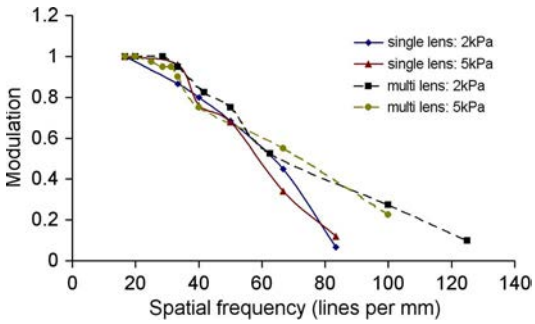

Fig. 16. Modulation of the grating using the single lens and the multilens system. The modulation is obtained from the OCT images of the grating with different periods. The x-axis is reciprocally related to the period of the grating.

distances, which would not be the case if the measurement head were to have a fixed focal length.

The lateral resolution may be quantitatively specified using a measurement of the MTF using this target. MTF is measured in this case by a measurement of the contrast between the glass and aluminum stripes for the different spacings (4 to 30 μm). Contrast ζ is found from

$$\zeta^T = \frac{I_{al}^T - I_{gl}^T}{I_{al}^T + I_{gl}^T} \tag{4}$$

where I_{gl}^T and I_{al}^T are the measured intensities of the OCT image for glass and aluminum, respectively, at a given grating period T. The contrast values are normalized to the result obtained for a 500 μm wide grating, a width much larger than the minimum lateral resolution of the OCT system. From these measurements, the MTF is then the plot of normalized contrast as a function of the spatial frequency.

Fig. 16 shows the measured MTF for two measurement head configurations: a single tunable lens and a fixed focal length/tunable lens pair, as discussed in Section IV. As can be seen in the figure, the MTF curves of the single lens drop faster than the curves for the multilens system, consistent with the MTF measurements of these lenses as standalone systems, shown in Fig. 7.

The extrapolated frequency at which the MTF drops to the half of its maximum value is 60 lines/mm for the single lens and 75 lines/mm for the multilens system. The lateral resolution,

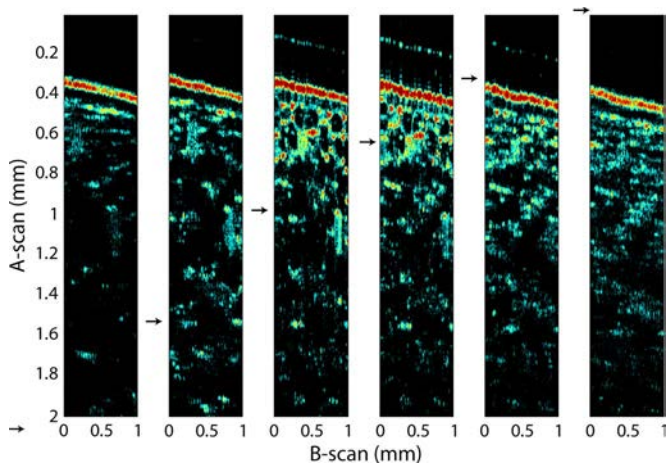

Fig. 17. Six cross-sectional images of an onion skin taken by B-scans using the same configuration as used for imaging the grating target. Each B-scan is done on the same slice with a new axial position of the focal point: the arrows indicate the approximate position of the focal point. Each B-scan comprises 200 A-scan.

defined as the reciprocal of the full width at half maximum (FWHM), is thus $\sim$17 μm for the OCT system with the tunable single microlens and $\sim$13 μm for the case of the tunable multilens system. However, the MTF multilens system drops more slowly than that of the single lens, indicating a high image contrast at high spatial frequencies.

B. Time-Domain OCT—Imaging

The same OCT configuration used in the previous section with the dual tunable lens system was used to obtain cross-sectional images of an onion skin. Since, as discussed in Section IV-B, the dynamic response of the tunable lens is insufficient to allow tuning concomitant with an A-scan in the kHz regime, the measurements were done at six distinct focal lengths to show the improvement in resolution for the depth region in the sample close to the focal point.

Fig. 17 shows the resultant six images; the arrows at the left of each image indicate the approximate position of the focal point. As can be seen in the leftmost image of the onion skin, the structures near the onion surface are poorly resolved, because they are far from the focus position. By moving from left to right in the figure, the focal point moves closer to the surface, and, therefore, more structures near the surface are resolved, whereas structures near the bottom start to disappear. An improved image quality is found at depths near the focal point.

Therefore, synchronizing the axial position of the beam waist concomitantly with the axial scan of the OCT results in improved image quality at all depths, demonstrating the benefit of a tunable objective in the measurement head.

C. En-Face OCT

In en-face OCT, the B- and C-scans are performed at high rates and the A-scan stepped layer-by-layer into the sample; for that reason, the A-scan is considerably slower than the B- and C-scans, allowing the tunable objective to shift the focal

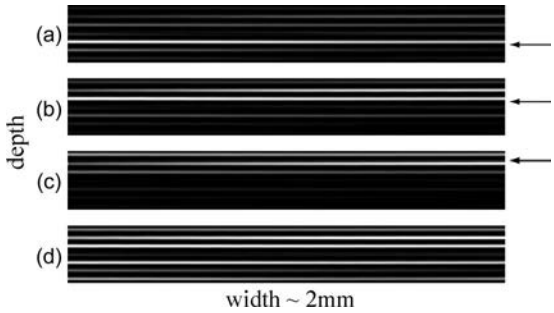

Fig. 18. Four en-face OCT images of a stack of 140 μm thick cover slides. The arrows on the right side (a)–(c) indicate the position of the fixed focal point. The last image (d) was obtained with focal point moving synchronously with the A-scan.

length concomitantly with the A-scan. The functionality of the tunable objective was thus evaluated in an en-face OCT setup by imaging a stack of 140 μm thick cover slides, where reflection from each interface provides a distinct OCT signal. The 2-D en-face images were obtained by taking a B-scan with a fixed position of the reference mirror, and thus measurement depth. After each B-scan, the reference arm was incremented in a 5 μm step, and the system takes the next B-scan.

Fig. 18 shows the resulting cross-sectional images of the cover slides using a B-scan of about 2 mm. As indicated by the arrows on the right side of the first three images (a–c), the measurement was performed with the focal point set at a fixed position. The last image (d) was then obtained with focal point moving synchronously with the slow axial scan.

As can be seen in the first three plots of the figure, the interfaces between the cover slides are only resolved in the depth near the position of focal point, corroborating the results of Fig. 17. Only in the last image, Fig. 18(d), are all the slides seen, since the focal point is scanned axially during the measurement. We see thus that in an en-face OCT system, the tunable objective may be may be synchronized with the A-scan and thus yield high-resolution images for a large depth range. The miniaturized scanning micromirror and the tunable microlens were also combined for use in the en-face configuration. The scanning mirror replaces the function of the translation stage in the previous experiment, and the tunable microlens is again used for the focal point tunability, synchronously with the slow A-scan. The top side of the cover slide stack used in the previous experiment was covered with an adhesive tape to realize a surface with higher scattering than is the case for bare glass. Fig. 19 shows the image of seven slides with a nearly constant contrast at all depths. The image demonstrates the ability of adapting the focal tuning with the axial scan, with an incorporation with the scanning micromirror. The image shows an extended axial resolution to 40 μm due to the dispersion involved by inserting the acousto-optic modulator in the reference arm.

D. Fourier-Domain OCT

In a FD-OCT system, the reflected signal from the measurement head interferes with the light reflected back from the reference arm. The resulting interferogram is incident onto a grating

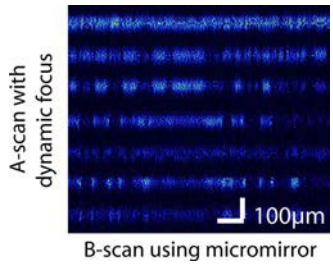

Fig. 19. En-face OCT image of a stack of 0.14 mm thick cover slides. The B-scan was carried out by the scanning micromirror, while the focal point was shifted synchronously with the slow A-scan.

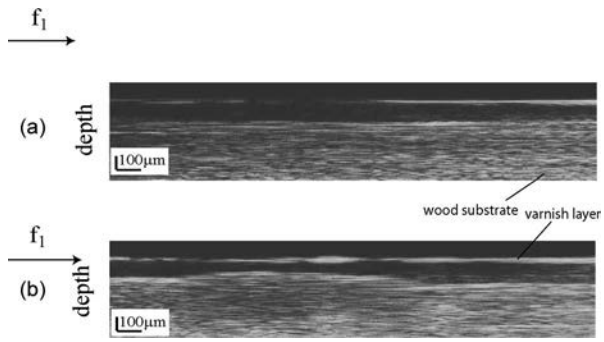

Fig. 20. OCT images of a varnish layer deposited on a wood substrate taken with a FD-OCT setup. A single 2 mm B-scan was performed and the focal point fixed at two positions, above the surface (f_1, in (a)) and on the surface (f_2, in (b)). Resolution of surface features is higher for the second case.

and the dispersed spectrum imaged by a 1-D photodetector array. The spatial Fourier transform of this signal then yields the depth-dependent reflection profile, such that no scan of the optical path length of the reference arm of the Michelson interferometer is necessary. The head was tested using a free-space implementation, and the measurements were with actuation of both micro-optical components, but not incorporated inside the miniaturized probe.

The 3-D scanning system based on the configuration of Fig. 11(a) was thus integrated into the sample arm of an FD-OCT setup. A slide of wood with a surface layer of varnish was used as a test sample. The advantage of the using the tunable objective in FD-OCT arrangement is the ability to tune the focal point to the desired depth in the sample before acquiring the image, thus allowing an improvement of the image at the depth corresponding to the position of the focal point.

The 2-D images obtained using a single B-scan by actuating the micromirror of the measurement head are shown in Fig. 20; the focus was fixed at two positions, above the surface (a) and at the level of the varnish layer (b). The axial position of the focus affects the detail resolved, as we have seen in the measurements of Figs. 17 and 18 using the other OCT systems: image quality is highest in the region near the focal point.

The generation of a complete 3-D OCT image is demonstrated in Fig. 21, in which the scanning mirror of the measurement head was used to generate the B- and C-scans; a biological sample, a leek skin, was used as a target. The tunable objective was used to position the focal point, once on the top of the sample (a) and once above the surface (b). The former case yields a more detailed view of the subsurface structures,

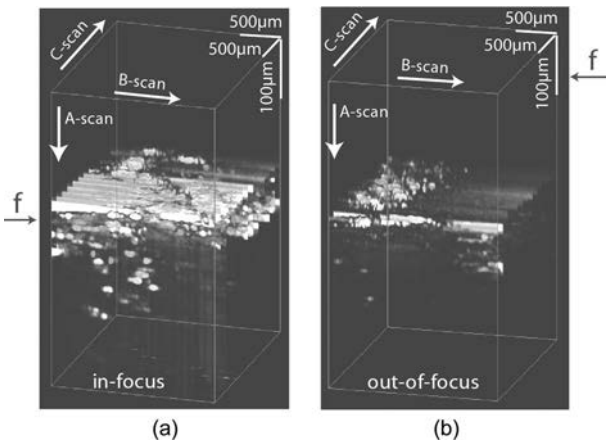

Fig. 21. 3-D FD-OCT images of a biological sample obtained using the scanning mirror of the measurement head. The focal point, indicated by the arrow in the figure, was placed (a) slightly below the target and (b) above the target, such that the latter is out of focus. Each image contains 13 B-scans and the imaging depth is approximately 300 μm. The lateral resolution of the complete system is ~ 16 μm.

whereas for the second, corresponding to an "out-of-focus" situation, the resolution is, as expected, considerably poorer.

The results of Fig. 21 show the performance advantages of the scanning measurement head with the tunable objective, particularly when used in an endoscopic implementation. Even though a FD-OCT setup generates an effective A-scan by means of the Fourier transform, proper positioning of the focal point on the axial axis is essential for enhanced lateral resolution and the image quality in general. The lateral resolution of the complete system is ~ 16 μm, based on the FWHM criterion. The tunable objective permits accurate placement of the operating focal point *in situ*, so that the imaging may be optimized independent of endoscopic measurement head position.

VIII. Current Limitations and Future Potential

There are a number of limitations of the current system which require further work to allow the system to be practically employed in endoscopic applications. For example, despite the successful reduction of the driving voltage below 100 μm for $\pm 4^\circ$, the voltage is still too high for *in vivo* use. One approach is to reduce the stiffness of the torsional mirror mounts, which can be accomplished through the use of softer materials, such as nickel. Alternatively, we are currently developing purely pneumatically actuated mirrors, which do not require high voltages at the distal end of the probe.

In addition, the tuning speed of the microlens is limited. Due to the high required lateral resolution, the microlens has a small depth-of-focus (DOF), which, however, requires a long tuning range, typically between 2 mm and 6 mm, for most applications. Finally, the assembly of the entire optical microoptical system still uses conventional fine mechanics technology, which is still dominant in commercial endoscopic manufacturing and assembly. An improved assembly method based on silicon-on-bench technology is currently in development, with which the probe diameter can be reduced and the optical alignment of the entire optical system improved.

IX. Outlook

The application of MEMS technology has allowed the realization of a miniaturized measurement head for OCT systems, incorporating a tunable objective and a two-dimensionally scanning micromirror. This system allows dynamic variation of the focal point and scanning of the measurement beam, in a system whose diameter of less than 4.5 mm permits integration into a standard rigid endoscope. Demonstration of its utility in TD, FD, and en-face OCT systems has shown that the optical performance of this measurement head, in particular the achievable lateral resolution, is promising for biological diagnostics.

Further developments in microsystems integration techniques will allow continued improvement in functionality with concomitant further reduction in size. Ongoing work will demonstrate an all-silicon system with only half of the currently demonstrated diameter and include the ability to generate 360° images about the circumference of the measurement head.

Acknowledgment

The authors are grateful to A. Fischer, now at KTH, Stockholm, for measurements of Fig. 10. They also thank A. Werber, D. Kallweit, D. Mader, B. Aatz, and J. Hoppe for their contributions to this work.

References

[1] W. Drexler and J. Fujimoto, Eds., *Optical Coherence Tomography: Principles and Applications*, 7th ed. New York: Springer-Verlag, 2008

[2] J. Singh, J. Teo, Y. Xu, C. Premachandran, N. Chen, R. Kotlanka, M. Olivo, and C. Sheppard, "A two axes scanning SOI MEMS micromirror for endoscopic bioimaging," *J. Micromech. Microeng.*, vol. 18, no. 2, p. 025 001 (9pp), Feb. 2008.

[3] W. Jung, D. McCormick, Y. Ahn, A. Sepehr, M. Brenner, B. Wong, N. Tien, and Z. Chen, "*In vivo* three-dimensional spectral domain endoscopic optical coherence tomography using a microelectromechanical system mirror," *Opt. Lett.*, vol. 32, no. 22, pp. 3239–3241, Nov. 2007.

[4] K. Gilchrist, R. McNabb, J. Izatt, and S. Grego, "Piezoelectric scanning mirrors for endoscopic optical coherence tomography," *J. Micromech. Microeng.*, vol. 19, no. 9, p. 095 012 (11pp), Sep. 2009.

[5] A. Jain, A. Kopa, Y. Pan, G. Fedder, and H. Xie, "A two-axis electrothermal micromirror for endoscopic optical coherence tomography," *IEEE J. Sel. Topics Quantum Electron.*, vol. 10, no. 3, pp. 636–642, May/Jun. 2004.

[6] W. Jung, D. McCormick, J. Zhang, L. Wang, N. Tien, and Z. Chen, "Three-dimensional endoscopic optical coherence tomography by use of a two-axis microelectromechanical scanning mirror," *Appl. Phys. Lett.*, vol. 88, no. 16, p. 163 901, Apr. 2006.

[7] H. Fu, Y. Leng, M. Cobb, K. Hsu, J. Hwang, and X. Li, "Flexible miniature compound lens design for high-resolution optical coherence tomography balloon imaging catheter," *J. Biomed. Opt.*, vol. 13, no. 6, p. 060 502, Nov./Dec. 2008.

[8] B. Qi, P. Himmer, M. Gordon, V. Yang, D. Dickensheets, and A. Vitkin, "Dynamic focus control in high-speed optical coherence tomography based on a microelectromechanical mirror," *Opt. Commun.*, vol. 232, no. 1–6, pp. 123–128, Mar. 2004.

[9] A. Divetia, T. Hsieh, J. Zhang, Z. Chen, M. Bachman, and G. Li, "Dynamically focused optical coherence tomography for endoscopic applications," *Appl. Phys. Lett.*, vol. 86, no. 10, p. 103 902, Mar. 2005.

[10] A. Podoleanu, J. Rogers, D. Jackson, and S. Dunne, "Three dimensional OCT images from retina and skin," *Opt. Express*, vol. 7, no. 9, pp. 292–298, Oct. 2000.

[11] A. Podoleanu, "Optical coherence tomography," *Brit. J. Radiol.*, vol. 78, no. 935, pp. 976–988, Nov. 2005.

[12] C. Hitzenberger, P. Trost, P. Lo, and Q. Zhou, "Three-dimensional imaging of the human retina by high-speed optical coherence tomography," *Opt. Express*, vol. 11, no. 21, pp. 2753–2761, Oct. 2003.

[13] J. Izatt, M. Hee, G. Owen, E. Swanson, and J. Fujimoto, "Optical coherence microscopy in scattering media," *Opt. Lett.*, vol. 19, no. 8, pp. 590–592, Apr. 1994.

[14] J. M. Schmitt, S. L. Lee, and K. M. Yung, "An optical coherence microscope with enhanced resolving power in thick tissue," *Opt. Commun.*, vol. 142, no. 4, pp. 203–207, Oct. 1997.

[15] R. Leitgeb, C. Hitzenberger, and A. Fercher, "Performance of Fourier domain vs. time domain optical coherence tomography," *Opt. Express*, vol. 11, no. 8, pp. 889–894, Apr. 2003.

[16] T. Schmoll, C. Kolbitsch, and R. Leitgeb, "Ultra-high-speed volumetric tomography of human retinal blood flow," *Opt. Express*, vol. 17, no. 5, pp. 4166–4176, Mar. 2009.

[17] S. Boppart, "Optical coherence tomography: Technology and applications for neuroimaging," *Psychophysiology*, vol. 40, no. 4, pp. 529–541, Jul. 2003.

[18] A. Werber and H. Zappe, "Tunable microfluidic microlenses," *Appl. Opt.*, vol. 44, no. 16, pp. 3238–3245, Jun. 2005.

[19] K. Yamashita, "Pneumatic endoscopy of the Eustachian tube," *Endoscopy*, vol. 15, no. 4, pp. 257–259, Jul. 1983.

[20] H. Itoh, A. Saika, H. Oka, A. Shiotani, T. Hara, S. Nishioka, K. Higashp, and M. Takatsuji, "Endoscopic dilatation therapy using a small caliber balloon for esophageal achalasia," *Dig. Endosc.*, vol. 10, no. 4, pp. 343–347, 1998.

[21] S. Chuah, T. Hu, K. Wu, P. Hsu, W. Tai, Y. Chiu, C. Lee, and C. Changchien, "Clinical remission in endoscope-guided pneumatic dilation for the treatment of esophageal achalasia: 7-year follow-up results of a prospective investigation," *J. Gastrointest. Surg.*, vol. 13, no. 5, pp. 862–867, May 2009.

[22] W. Zhang, K. Aljasem, H. Zappe, and A. Seifert, "Highly flexible MTF measurement system for tunable micro lenses," *Opt. Express*, vol. 18, no. 12, pp. 12 458–12 469, Jun. 2010.

[23] D. Kallweit and H. Zappe, "Fabrication of bulk-Si micromirrors with an integrated tilt sensing mechanism," *J. Micromech. Microeng.*, vol. 16, no. 2, pp. 463–469, Feb. 2006.